Chapter 4: Stability and Design Studies of Periodically Dielectric Loaded Gyro-twystron Amplifier*

*Part of this work has been published as:

A. S. Singh and M. Thottappan, "Stability Study in Dielectric Ring Loaded Periodic Interaction Structure for a Megawatt Class Gyrotwystron," *IEEE Transactions on Electron Devices,* vol. 65, no. 10, pp. 4585 - 4591, Oct. 2018.

4.1 Introduction

The multimode study of unloaded gyro-twystron [103] has been carried out in chapter 2 and 3 using the nonlinear theory and CST particle studio, respectively. These studies predicted that the second harmonic TE_{02} mode is the most troublesome mode. In the present chapter, the interaction structure of gyro-twystron is designed to suppress the spurious second harmonic TE_{02} mode. Backward wave oscillations and instabilities of gyro-TWA are investigated using the linear theory and calculations are made to design oscillation tolerant structures.

In the present chapter, the origin of BWOs and their suppression techniques in a MW class gyro-twystron is studied. In section 4.2, the design methodology of each section of the RF structure is developed independently, and the issues related to the amplifier's stability in its output waveguide are discussed. In section 4.3, the nonlinear behavior of a PDL gyro-twystron is discussed, and the conclusion is drawn in section 4.4.

4.2 Design Methodology

4.2.1 Pre-bunching section

The design methodology of gyro-twystron includes the desired RF output power and stability constraints at its output section. The dimension of RF interaction structure primarily depends on the operating frequency and mode. The radius of the RF interaction structure is calculated by $r \geq x_{mn}\lambda/2\pi$, where, x_{mn} is Eigenvalue of TE_{mn} mode, and λ is the operating wavelength. The radius of the input cavity is chosen to support the operating frequency and mode, minimize the space charge effect and wall losses. The input cavity is designed to optimize the complex gain function, which is a measure of the susceptibility of the electron beam to the RF wave [61]. For reducing the initial oscillations in the RF output power, the quality factor of the input cavity is lowered [67] by loading it with a

lossy dielectric material. This allows the cavity to operate below the start oscillation current (SOC) and ensures the stable operation [9]. In the present design, the optimum quality factor of 260 is chosen to minimize the oscillations, whereas for a higher value of quality factor the beam current is well below the SOC (Figure 4.1). Unlike the input cavity, the radius of the drift tube is chosen to provide cut-off to the desired operating mode. The length of the drift tube is calculated from the cold cavity dispersion relation that provides sufficient isolation between the cavity and waveguide. The length (L_d) of the drift section is calculated as $L_d > 5.75 \Big/ \left[x_{mn}/r_d \right]^{2} - \omega/c \Big]^{1/2}$, where, the drift tube radius (r_d) follows the inequalities including $r_d < x_{mn}\, \lambda/2\pi$ and $r_g < r_d < r_{cav}, r_{w\ \min}$, r_g is the guiding centre radius, r_{cav} is the radius of the cavity, and r_w is the radius of the waveguide. In gyro-twystrons, the beam-wave interaction takes place in the waveguide section, and its design is very crucial at higher operating power due to the instability problem.

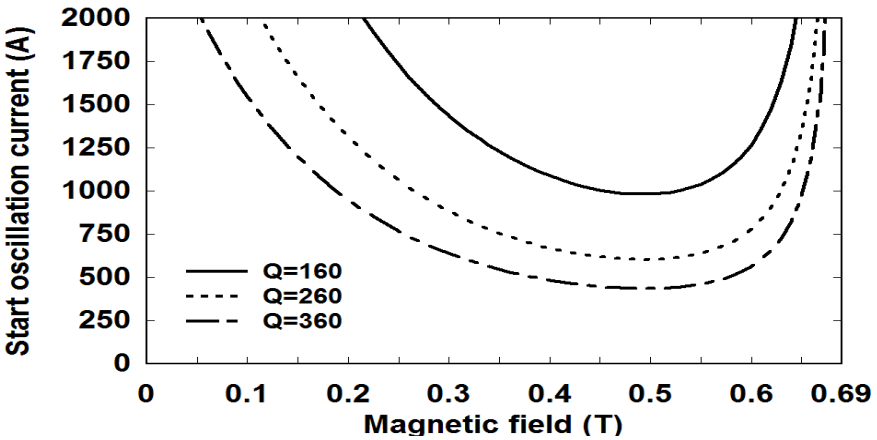

Figure 4.1 Variation of SOC with the magnetic field at the input cavity.

4.2.2 Analysis of parasites

The length of the waveguide is chosen below the start oscillation length of backward competing modes. The interaction between the RF signal and electron beam is discussed through small-signal dispersion equation gives instability, which may identified as

convective instability or absolute instability. Gyro-TWA operate near grazing point intersection, i.e. convective instability. For each operating current, there is a maximum limit in the length of RF interaction region that is known as a start oscillation length, above which backward wave oscillation starts. Similarly, for a definite interaction length there is a critical threshold current, which is called as start oscillation current above which the convective instability of Gyro-TWA turns into an absolute instability. The occurrence of instability is confirmed by solving small signal dispersion equation of the travelling wave section is given as

$$D(\omega, k_z) = \frac{\omega^2}{c^2} - k_z^2 - k_{mn}^2 - \frac{4I_b}{r_w^2 K_{mn} I_a}\left[\begin{array}{l} \dfrac{-\beta_{t0}^2\left(\omega^2 - k_z^2 c^2\right) H_{sm}(x,y)}{\left(\omega - k_z v_z - s\Omega/\gamma_0\right)^2} \\ + \dfrac{\left(\omega - k_z v_z\right) T_{sm}(x,y)}{\left(\omega - k_z v_z - s\Omega/\gamma_0\right)} - \dfrac{\left(k_{mn} v_{t0}\right) U_{sm}(x,y)}{\left(\omega - k_z v_z - s\Omega/\gamma_0\right)} \end{array}\right] = 0 \quad (4.1)$$

where, , $K_{mn} = J_m^2\left(x_{mn}\right)\left(x_{mn}^2 - m^2\right)/x_{mn}^2$, ω is angular frequency, k_z is the axial wave number, $k_{mn} = x_{mn}/r_w$, x_{mn} is the nth root of $J_m'\left(x_{mn}\right) = 0$, β_{to} is initial normalized transverse velocity component, I_b is the beam current, $I_a \approx 17\beta_{zo}\gamma_0$ kA is Alfven's current, Lorentz factor $\gamma_0 = \left(1 - \beta_z^2 - \beta_t^2\right)^{-1/2}$, cyclotron frequency, $\Omega = eB_0/m_e$, r_w, r_g, and rL are waveguide radius, guiding centre radius, and Larmor radius, respectively. H_{sm} term is a measure of the coupling between the transverse motion of electrons and RF signal, i.e. azimuthal bunching, T_{sm} term is the measure of the coupling between RF signals and pondermotive force, i.e. axial bunching and last U_{sm} term is a measure of the electron guiding centre drift, which are expressed as,

$$H_{sm}(x,y) = J_{s-m}^2(x) J_s'^2(y) \quad (4.2)$$

$$T_{sm}(x,y)=2H_{sm}(x,y)+yJ_s^{'}(y)$$
$$\left\{2J_{s-m}^2(x)J_s^{''}(y)-J_s(y)\left[\frac{1}{x}J_{s-m}(x)J_{s-m}^{'}(x)+J_{s-m}^{'2}(x)+J_{s-m}(x)J_{s-m}^{''}(x)\right]\right\} \quad (4.3)$$

$$U_{sm}(x,y)=-\frac{1}{2}yJ_s^{'}(y)\begin{Bmatrix}J_{s-1}(y)\left[J_{s-m-1}^2(x)-J_{s-m}^2(x)\right]-\\J_{s+1}(y)\left[J_{s-m+1}^2(x)-J_{s-m}^2(x)\right]\end{Bmatrix} \quad (4.4)$$

where, $x=k_{mn}r_g$, $y=k_{mn}r_L$.

For lossy waveguide, $k_{mn}\to k_{mn}\left[1-(1-j)\left(\left(x_{mn}^2/x_{mn}^2-m^2\right)\left(\omega^2/\omega_c^2\right)\right)s_d/r_w\right]$, where s_d is skin depth of lossy material.

$$F(z)=F(0)\sum_i\frac{N(k_{zi})e^{-jk_{zi}z}}{jD^{'}(k_{zi})}+F^{'}(0)\sum_i\frac{e^{-jk_{zi}z}}{jD^{'}(k_{zi})} \quad (4.5)$$

where, $D^{'}(k_z)=dD^{'}(k_z)/dk_z$, $N(k_z)=S_0(k_z)-jk_z$ and k_{zi} is the root of the dispersion equation $\left(\frac{\omega}{c}\right)^2-k_z^2-k_{mn}^2-S_1(k_z)=0$.

$$S_1(k_z)=-\frac{16\pi^3e^2kk_{mn}C_{mn}^2}{m_0c^2}\sum_{s=-\infty}^{\infty}\int_0^{r_{g\max}}r_bdr_b\int_0^{\infty}p_{\perp}dp_{\perp}\int_{-\infty}^{\infty}dp_z\,f_0/\gamma$$
$$\left[\frac{-\beta_{t0}^2\left(w^2-k_z^2c^2\right)H_{sm}(x,y)}{\left(\omega-k_zv_z-s\Omega/\gamma_0\right)^2}+\frac{(\omega-k_zv_z)T_{sm}(x,y)}{(\omega-k_zv_z-s\Omega/\gamma_0)}-\frac{(k_{mn}v_{t0})U_{sm}(x,y)}{(\omega-k_zv_z-s\Omega/\gamma_0)}\right] \quad (4.6)$$

$$S_0(k_z)=-\frac{16\pi^3e^2kk_{mn}C_{mn}^2}{m_0c^2}\sum_{s=-\infty}^{\infty}\int_0^{r_{g\max}}r_gdr_g\int_0^{\infty}p_tdp_t\int_{-\infty}^{\infty}dp_z\,\frac{f_0}{\gamma}\left[\begin{array}{c}\dfrac{-c\beta_{t0}^2k_zH_{sm}(x,y)}{\left(\omega-k_zv_z-s\Omega/\gamma_0\right)^2}\\+\dfrac{\beta_zT_{sm}(x,y)}{\left(\omega-k_zv_z-s\Omega/\gamma_0\right)}\end{array}\right] \quad (4.7)$$

The following boundary conditions are applied to solve the field equations with respect to axial length [104]. For a forward wave $\left(\mathrm{Re}(k_z)>0\right)$

$$|F(0)|=\sqrt{\omega k_{mn}^2P_{\omega}(0)/k_z}\text{, and } F^{'}(0)_{z=0}=-jk_zF(0) \quad (4.8)$$

For a backward wave $\left(\mathrm{Re}(k_z)<0\right)$

$$F^{'}(0)_{z=0}=jk_zF(0)\text{, and } \mathrm{Re}\{F(z)\}+j\,\mathrm{Im}\{F(z)\}=0,\quad (z=L) \quad (4.9)$$

4.2.3 Design of dielectric-loaded section

For stable operation, the interaction length is kept below the critical length of BWO modes. However, to achieve the desired RF output power and increase the device gain, the interaction length should be long enough that is realized by introducing lossy structures. The PDL is a distributed loss technique that has been employing in gyro-TWA to achieve the stability against spurious oscillations. The RF interaction structure comprises lossy rings, which are axially separated by vacuum gaps and partly fit into the grooves on the inner surface of the metallic waveguide to maintain periodicity tolerances. The metal septum on either side of the dielectric ring reduces the halo formation due to stray electrons and acts as beam scrapers. The metal cylindrical waveguide having the radius of r_w is loaded with periodic dielectrics having the radial thickness of 'r_{th}' and an axial thickness of 'w_d' (Figure 4.2). The interspacing between the two consecutive dielectric rings are 'w_v' with the periodicity of 'L'. The radial thickness of the dielectric ring is, $r_{th} = r_m - r_{dl}$, that divides the RF circuit into three regions (Figure4.2), where r_m and r_{dl} are the outer and inner radius of the dielectric ring, respectively. The region R_I ($0 < r < r_{dl}$, $0 < z < \infty$), is the ring free region, the dielectric ring alone is region R_{II} ($r_{dl} \leq r < r_m$,$0 < z \leq w_d$) and the region, R_{III} ($r_{dl} \leq r < r_w$, $w_d + w_m < z < L$)), is created due to the duct between alternating dielectric rings. At the metallic boundary the tangential electric field required to be zero, i.e., the azimuthal electric field is zero ($E_\Phi = 0$). Similarly, the azimuthal electric field also be zero at the infinitesimally thin metal interface ($z = w_m$).

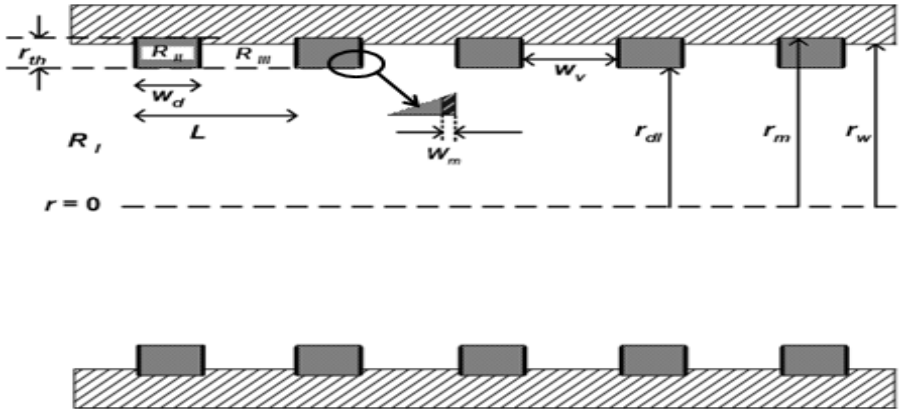

Figure 4.2 The longitudinal view of PDL waveguide.

The boundary conditions at the interface between these regions are given as,

At $r = r_{dl}$

$$H_z^I = H_z^{II} \text{ and } E_\varphi^I = E_\varphi^{II}; \qquad \text{for } 0 < z < w_d$$

$$H_z^I = H_z^{III} \text{ and } E_\varphi^I = E_\varphi^{III}; \qquad \text{for } w_d + w_m < z < L$$

$$E_\varphi^{II} = E_\varphi^{III} = 0; \qquad \text{at } z = w_m$$

$$\text{At } r = r_m \; E_\varphi^{II} = 0; \qquad \text{for } 0 < z < w_d$$

$$\text{At } r = r_w \; E_\varphi^{III} = 0; \qquad \text{for } w_d + w_m < z < L$$

The mathematical formalism of PDL waveguide is derived from Floquet's theorem and mode-matching technique. Since the RF circuit is loaded periodically, Floquet's theorem can be expanded as a sum of Bloch or longitudinal components of the field having azimuthal symmetry. For region R_I, the fields are given as [105],

$$H_z^I = \sum_{a_I=-\infty}^{\infty} A_{a_I}^I J_0\left(h_{a_I}^I r\right) e^{j\omega t - jk_{a_I} z} \tag{4.10}$$

$$E_\varphi^I = j\omega\mu_0 \sum_{a_I=-\infty}^{\infty} \frac{1}{h_{a_I}^I} A_{a_I}^I J_0'\left(h_{a_I}^I r\right) e^{j\omega t - jk_{a_I} z} \tag{4.11}$$

where, $h_{a_I}^{I\ 2} = \omega / c^{\ 2} - k_{a_I}^2$ is the transverse wave number, $k_{a_I} = k_0 + 2\pi a_I / L$ is the axial wave number, a_I is the space harmonic number and A_q^I is the coefficient term in region R_I. Similarly, the field components in region R_{II} are given as [105],

$$H_z^{II} = \sum_{a_{II}=1}^{\infty} A_{a_{II}}^{II} G_0\ \ h_{a_{II}}^{II} r\ \ \sin(a_{II}\pi z / \mathrm{w}_d) e^{j\omega t} \tag{4.12}$$

$$E_\varphi^{II} = j\omega\mu_0 \sum_{a_{II}=l}^{\infty} \frac{1}{h_{a_{II}}^{II}} A_{a_{II}}^{II} G_0^{'}\ \ h_{a_{II}}^{II} r\ \ \sin(a_{II}\pi z / \mathrm{w}_d) e^{j\omega t} \tag{4.13}$$

where, $G_0\ \ h_{a_{II}}^{II} r\ = J_0\ \ h_{a_{II}}^{II} r\ \ Y_0^{'}\ \ h_{a_{II}}^{II} r_w\ - Y_0\ \ h_{a_{II}}^{II} r\ \ J_0^{'}\ \ h_{a_{II}}^{II} r_w$, $h_{a_{II}}^{II\ 2} = \omega / c^{\ 2} \varepsilon_r - (k_{a_{II}}^{II})^2$ is the transverse wave number, $k_{a_{II}}^{II} = \pi a_{II} / w_d$ is the axial wave number, a_{II} is the modal harmonic number in the dielectric region, R_{II} and $A_{a_{II}}^{II}$ is the coefficient term in region R_{II}. The field components developed in the duct region R_{III},are described as [105],

$$H_z^{III} = \sum_{a_{III}=1}^{\infty} \left[A_{a_{III}}^{III} J_0^{'}\ \ h_{a_{III}}^{III} r\ + B_{a_{III}}^{III} Y_0^{'}\ \ h_{a_{III}}^{III} r\ \ e^{j\omega t} \right] \sin\ \ a_{III}\pi z / \mathrm{w}_v\ \ e^{j\omega t} \tag{4.14}$$

$$E_\varphi^{III} = j\omega\mu_0 \sum_{a_{III}=1}^{\infty} \frac{1}{h_{a_{III}}^{III}} \left[A_{a_{III}}^{III} J_0^{'}\ \ h_{a_{III}}^{III} r\ + B_{a_{III}}^{III} Y_0^{'}\ \ h_{a_{III}}^{III} r\ \ e^{j\omega t} \right] \sin\ \ a_{III}\pi z / \mathrm{w}_v\ \ e^{j\omega t} \tag{4.15}$$

where, $h_{a_{III}}^{III\ 2} = \omega / c^{\ 2} - k_{a_{III}}^2$ is the transverse wave number, $k_{a_{III}} = \pi a_{III} / w_v$ is the axial wave number, a_{III} is the modal harmonic number in vacuum gap R_{III} and $A_{a_{III}}^{III}, B_{a_{III}}^{III}$ are the coefficients in region R_{III}. The partial penetration of wave into the lossy dielectric rings (Region-II) forms the standing wave in it and between the infinitesimally thin metal rings (Region-III). To represent the standing wave field in region II and region III, the modal harmonics are considered [42]. The field intensity equations (4.10) - (4.17) are used to study the propagation characteristics in various region of RF structure. The normalized

azimuthal electric field distribution in both dielectric and vacuum regions have been plotted by considering the *modal/standing* wave and *space/Bloch* harmonics, respectively. The normalized amplitude in the vacuum region (R_I) (Figure 4 (a)) is calculated by considering space harmonics in that region and equation (4.10) – (4.11). This shows that the field is maximum for the fundamental space harmonic ($a_I = 0$) and decreases on either side of the peak, i.e. for higher Bloch harmonics, the amplitude of the field is attenuated in the vacuum region. Similarly, in the dielectric region (R_{II}) the normalized amplitude (Figure 4 (b)) is calculated using *modal harmonics* and equation (4.12) – (4.13) with the normalization factor, $\omega \times \mu_o$ / 1.053×10^3. It is observed that the amplitude of the electric field decreases as the modal harmonic number increases, i.e., higher standing wave harmonic component of the field in the dielectric region is suppressed.

The dispersion of the present PDL waveguide is plotted and compared with the dispersion of unloaded waveguide (Figure 4.4). This is obtained by reducing the axial wave number at fundamental space harmonic ($a_I = 0$), i.e. for the real values of axial wave number. For the fundamental harmonic, $k_{a_I} = k_0$ where, $k_{a_I} = k_0 + 2\pi a_I / L$ and $h_{a_I}^{I\ 2} = \omega / c^{\ 2} - k_0^2$. The physical dimensions of the dielectric-loaded waveguide section depend on the transmission losses of the desired and spurious BWO modes, SOC, critical length, etc. The SOC and critical length of the operating mode can be increased using lossy RF interaction structures [106]. The SOC (I_s) is given by [106],

$$I_s = 2k_b^4 \Big/ C_{mn} C_j k_c^4 \ \ 0.00112\, L_{dB} / L_{wg}^{\ \ 3} \ 1 + 1013 \Big/ L_{dB}^2 \Big)^3 \qquad (4.18)$$

where, $C_{mn} = J_{s-m}^2\ x_{mn} r_g / r_w\ \Big/ J_m^2\ x_{mn}\ \ x_{mn}^2 - m^2$ is coupling coefficient, $C_j = 2.348\times10^{-4}/\gamma\beta_z\ \ \beta_t/\beta_z\ ^2\ \ J_1'\ \ \beta_t\omega_c/\Omega$ is a constant, L_{wg} is the length of the waveguide, L_{dB} is the transmission loss in dB, $k_c = \omega_c/c$ is cut-off wave number, $k_b = \ \omega-\Omega\ /v_z$ is the beam wave number, Ω is the cyclotron frequency, γ is the relativistic mass factor, ω_c is the angular cut-off frequency, and β_t and β_z are the normalized transverse and axial velocities of electrons, respectively.

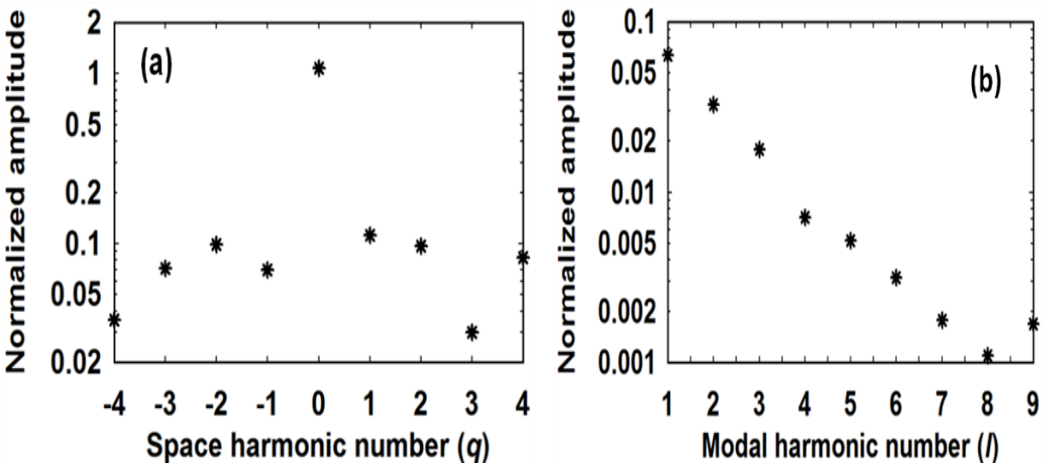

Figure 4.3 Normalized azimuthal electric field variation over (a) space harmonic number in vacuum region (b) modal harmonic number in the dielectric region.

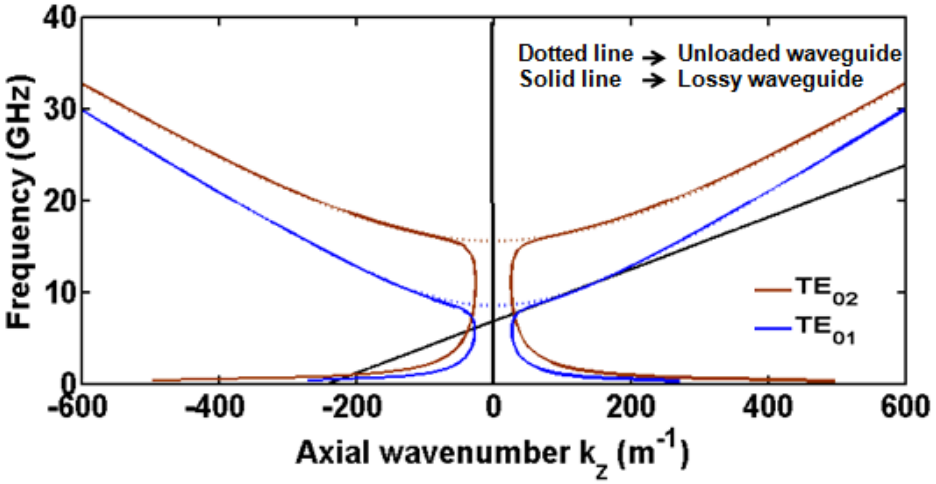

Figure 4.4 Dispersion of lossy PDL gyro-twystron amplifier

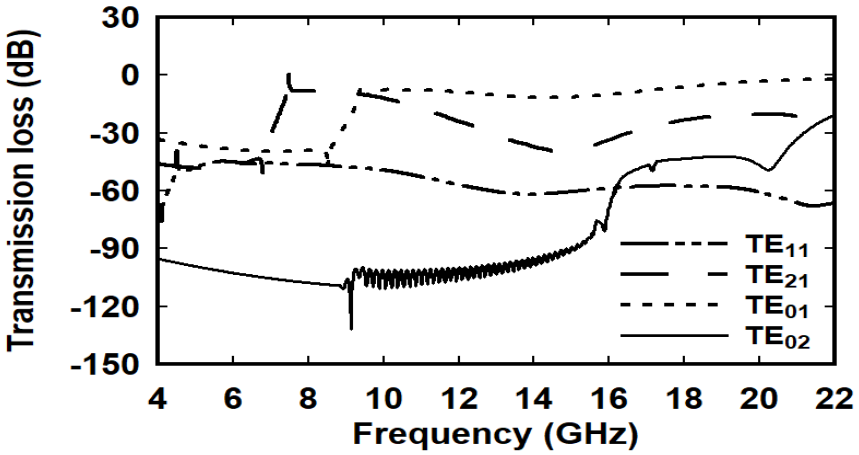

Figure 4.5 Propagation loss as a function of frequency for dielectric waveguide (complex permittivity of BeO-SiC is 31-13j).

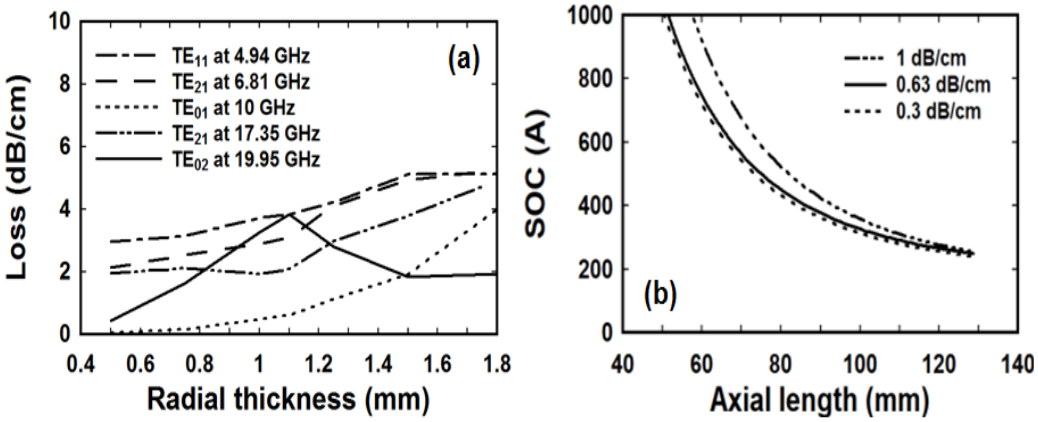

Figure 4.6 Propagation loss Vs radial thickness of the dielectric material and (b) SOC Vs axial length for operating TE_{01} mode.

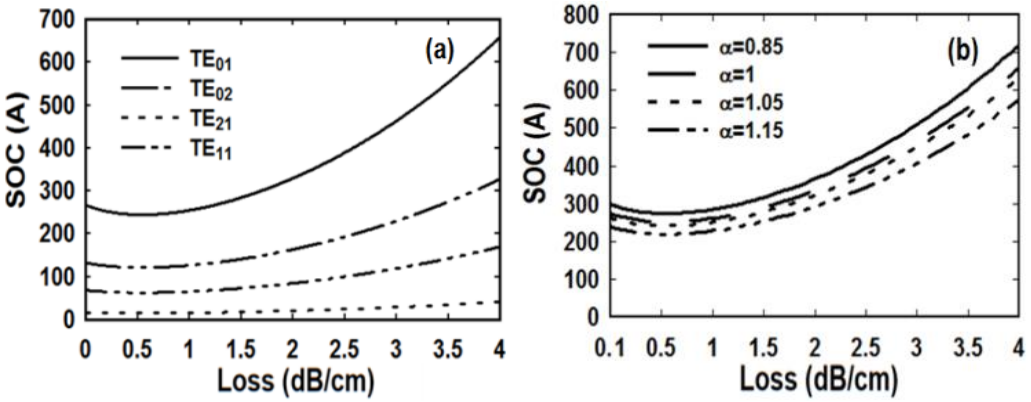

Figure 4.7 (a) SOC variation with the loss for different modes and (b) SOC variation with propagation loss for different beam-velocity pitch factor.

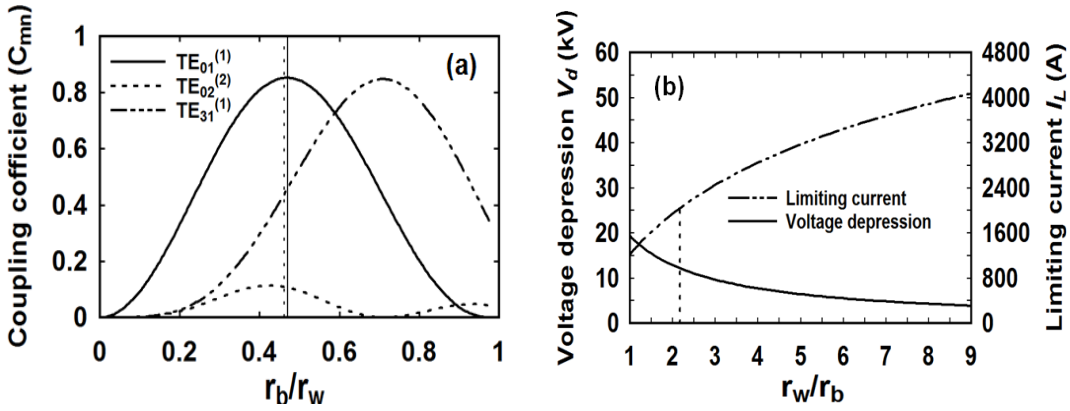

Figure 4.8(a) Coupling coefficient variation with the ratio of the beam to waveguide radii (b) variations in the depressed voltage and limiting current with the ratio of the waveguide to beam radii (at r_w=19.5mm).

Table 4.1 Design parameters of PDL gyro-twystron

Particulars	Values
Beam Voltage	440 kV
Beam Current	220 A
Beam-velocity pitch factor	1.0
Velocity spread	4%
Pre-drift section length	32 mm
Input cavity radius	28.1 mm
Input cavity length	17.3 mm
Drift section radius	15 mm
Drift section length	143.6 mm
Waveguide radius	19.5 mm
Unloaded Waveguide length	125 mm
Loaded Waveguide length	125 mm
Guiding centre radius	0.4615 r_w

To achieve the stability against parasites in gyro-twystron, its output section is loaded axially with periodic dielectric rings. The cold dispersion calculation of PDL waveguide is predicted the attenuation of 0.63dB /cm for the desired TE_{01} mode at 10GHz. Similarly, the loss per unit length of other parasites including TE_{11}, TE_{21}, and $TE_{02}^{(2)}$ is calculated as ~3.84dB /cm at 4.94GHz, ~3.1 dB /cm at 6.81GHz, and 3.68dB /cm at 19.95GHz, respectively (Figure 4.5). This calculation clearly shows that the attenuation of all parasites is larger than that for the desired TE_{01} mode as required. The dependence of loss per unit length on the radial thickness of the dielectric is shown in Figure 4.6(a). In the

present design, the radial thickness of the dielectric ring has been optimized as 1.1mm to achieve stability against parasites. The SOC analysis needs to consider the loss per unit length of the desired and parasitic modes. The SOC of operating TE_{01} mode is decreasing along the axial length of the RF circuit (Figure 4.6(b)). For the loaded length of 125mm, the SOC approaches to 255A for the loss per unit length of 0.63dB /cm. The loaded waveguide with the loss per unit length of 0.3 dB /cm shows the lowest SOC of 250A while the SOC for the loss per unit length of 1dB /cm approaching ~265A (Figure 4.7(a)). It shows that the SOC of the desired TE_{01} mode is in the range of 250-270A for the loss per unit length < 1dB /cm. Hence, the dielectric loading increases the SOC of operating TE_{01} mode significantly as compared to the BWO modes. From the SOC analysis, the operating point is chosen below 250A for the stable operation of the device.

4.2.4 Beam Present Design Issues

Electron beam parameters like beam-velocity pitch factor, guiding centre radius, etc. are optimized to increase the beam-wave interaction efficiency of PDL gyro-twystron. The sensitivity of SOC with respect to loss is studied (Figure 4.7(b)). It is observed that the SOC decreases as the beam-velocity pitch factor increases for the desired loss per unit length. As the beam-velocity pitch factor approaches 1.05, the SOC falls below 236A. In the present design, obviously the operating current should be below the SOC (250A). Therefore, to maintain stability unity beam-velocity pitch factor is chosen that is well below the limiting value. The large wall radius of interaction structure is required to accommodate the large radius of the electron beam without any interception. As a measure of beam-wave interaction strength, the coupling coefficient that has an inverse linear relation with the SOC is investigated. The position of the guiding center radius is chosen to maximize the coupling of the electron beam with the desired mode of the RF signal. The coupling coefficient given in Figure 4.8(a) shows that the desired operating

TE_{01} mode has the maximum coupling at r_g/r_w=0.47, which is slightly above the selected beam radius of 9 mm. The space charge effect due to the electron beam present in RF interaction structure that causes the spread in beam energy and reduces amplifier efficiency. The space charge effect is minimized by keeping the voltage depression less than 10 % of the beam voltage and limiting current should be more than twice of the beam current. The voltage depression of 12.14kV and limiting current of 2000A is obtained at r_w/r_g= 2.17 (Figure 4.8(b)), and the space charge effect is well below for the operating beam voltage and current.

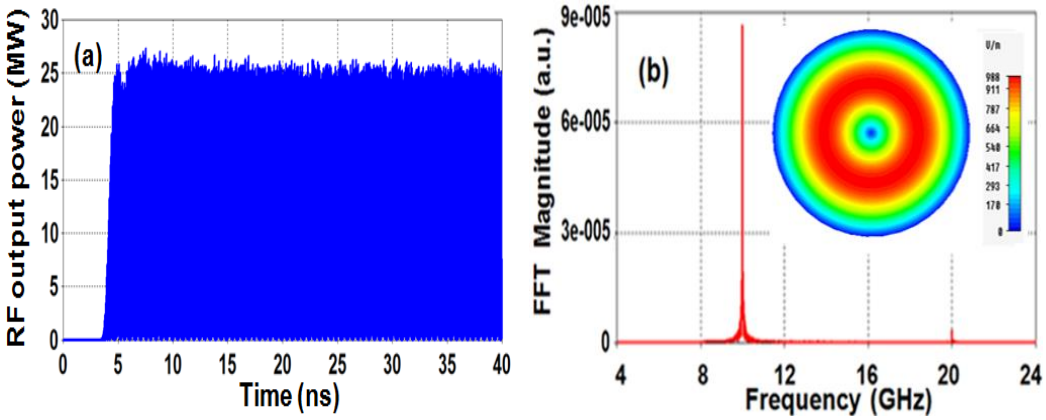

Figure 4.9 (a) Temporal variation of RF output power and (b) spectrum of output signal and contour (inner figure) of desired TE_{01} operating mode (at 4% of velocity spread).

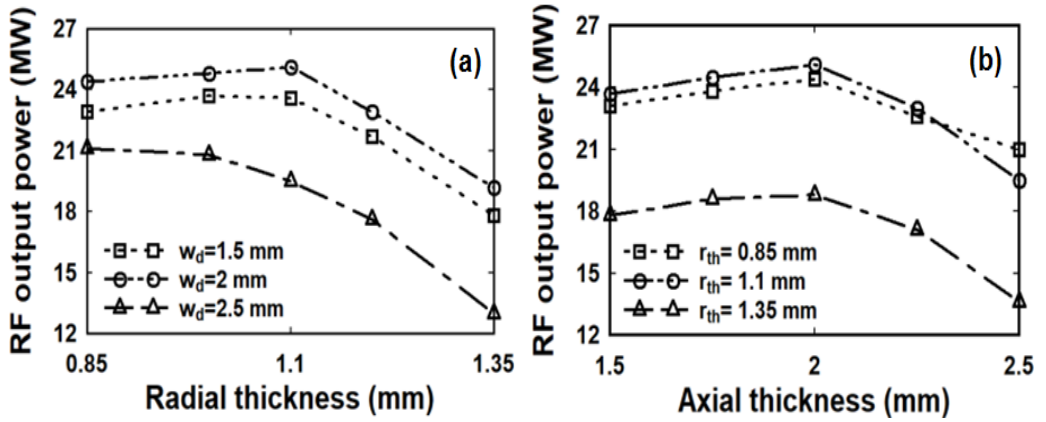

Figure 4.10 RF output power Vs (a) radial thickness (b) length of dielectric rings (complex permittivity is 31-13j).

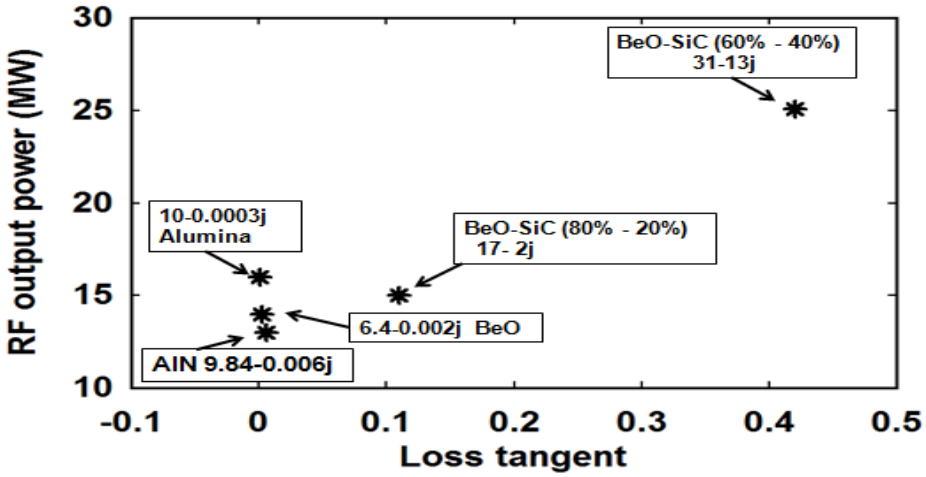

Figure 4.11 RF output power Vs loss tangent for practical dielectrics *(for fixed r_{th}=1.1 mm and w_d=2mm).*

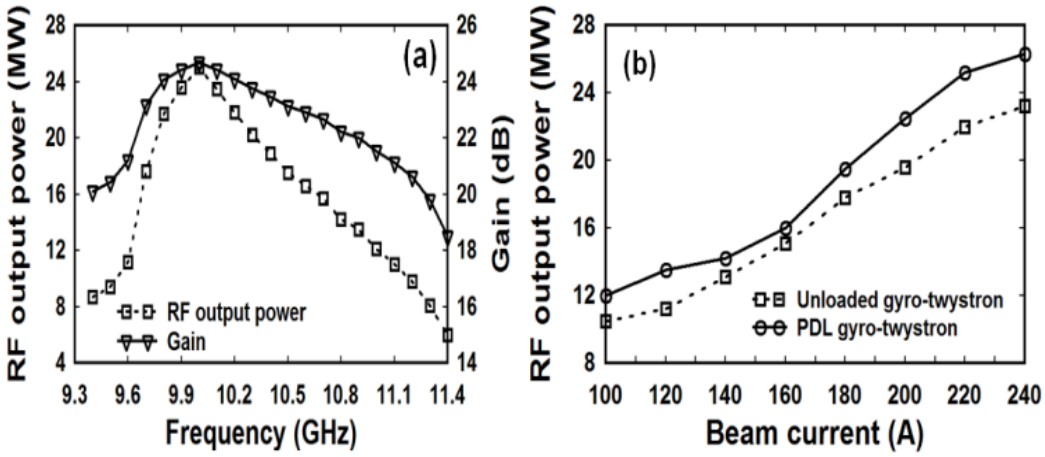

Figure 4.12(a) RF output power variation over the frequency (b) RF output power variation over the beam current (for fixed RF input of 85kW).

4.3 Results and Discussion

The small-signal theory is used to investigate the spurious parasites or BWOs, as discussed in section II, which brings out the RF circuit and electrical design parameters, as shown in Table 4.1. The physics of nonlinear amplification or transient behaviour of PDL gyro-twystron is investigated using a commercial 3D simulation code [96]. The 3D simulation of the present amplifier predicted a saturated output of ~25 MW in TE_{01} mode (Figure 4.9(a)). The frequency spectrum of the developed output signal at 10 GHz is shown in Figure 4.9(b) along with the pattern of desired TE_{01} mode. The geometry of dielectric material, including its radial thickness and axial thickness are optimized to

maximize the RF output power (Figure 4.10). The maximum RF power of ~25 MW is observed for the radial thickness of 1.1 mm and the axial thickness of 2mm while fixing other parameters (Figures. 4.10(a) and 4.10 (b)), respectively. To maintain the periodicity tolerance in the PDL RF structure, the dielectric rings are inserted/fitted into the metallic grooves having the depth of 0.2 mm. Further, the dielectric properties of practically possible different ceramic composites including BeO (60 %) – SiC (40 %), BeO (80 %) - SiC (20 %), BeO, AlN and Alumina are studied to maximize the RF output power (Figure 4.11). It was observed that the gyro-twystron loaded with a dielectric of BeO (60 %) – SiC (40 %) having the complex permittivity of 31-13j at 10 GHz predicted a maximum RF output of ~25 MW (Figure 4.11). After optimising the geometry and dielectric properties of rings, the sensitivity of RF output power on electrical parameters, including frequency and beam current is observed. Figure 4.12 (a) shows that the maximum RF output power of ~25 MW is achieved at the desired operating frequency of 10GHz with the maximum gain of 24.7 dB. The RF output power starts decreasing as moving away from the operating frequency due to the increase in the mismatch between operating frequency (ω) and cyclotron frequency (Ω)for a fixed velocity spread of 4 %. The performance of the PDL gyro-twystron is observed over the beam current while fixing all other design parameters, (Figure 4.12 (b)). This is compared with its unloaded counterpart (Figure 4.12 (b)), which shows that the distributed loss technique in the present gyro-twystron enhances the RF output by suppressing the parasites.

4.4 Conclusion

In the present chapter, the stability and design issues of X-band gyro-twystron using a PDL waveguide as its RF output section have been discussed. The lossy dielectric ring has the tendency to attenuate all spurious BWOs including TE_{11}, TE_{21}, and $TE_{02}^{(2)}$ modes,

consequently the stability of the amplifier was achieved. The influence of circuit and electrical design parameters over the performance of PDL gyro-twystron has been extensively studied through the simulation investigation. The PDL gyro-twystron developed a saturated RF output power of ~ 25 MW in the desired TE_{01} mode for a gyrating beam of 440 kV, 220 A with unity beam-velocity pitch factor and velocity spread of 4 %. In general, the spread in particle kinematics depends upon the DC space charge effect and increases with the DC input power. The conversion efficiency of the amplifier has been calculated as ~ 26 % and the power gain as ~24.7 dB. Further multimode behaviour in PDL waveguide of gyro-twystron will be investigated in the next chapter including the design and simulation RF coupling section.